Kinematic and experimental aerodynamic characterisation of the RotaFlap – a novel flapping wing mechanism

A. Ania
Department of Mechanical and Aerospace Engineering
Royal Military College of Canada
Ontario
Canada

D. Poirel
poirel-d@rmc.ca
Department of Mechanical and Aerospace Engineering
Royal Military College of Canada
Ontario
Canada

M.-J. Potvin
Space Technologies
Canadian Space Agency
Quebec
Canada

ABSTRACT

A unique patented mechanism, termed 'RotaFlap', which can move its wings in a figure-eight shape kinematically similar to insects or hummingbirds, has been investigated through the design, construction, integration and testing of various prototypes. In this paper, the most recent prototype is presented whereby the RotaFlap kinematics is characterised to understand some of its most pertinent parameters. A host of variations have been identified and in this study a subset of these have been tested. A preliminary characterisation of the force production, especially the vertical lift coefficient, has been completed. It is concluded that this mechanism produces vertical lift coefficient values similar to insect and hummingbird flight for similar Reynolds numbers.

NOMENCLATURE

c	chord length
$\bar{c}$	mean chord.
c_{max}	maximum chord length
CF_r	coefficient of resultant force, $Fr_{xyz}/(1/2\rho \bar{U}_t^2 S)$
d	wing arm distance, from the axis of rotation of the rectangular gearbox to the wing base
D	drag force (relative to the wing flight path)
f	flapping frequency
F_i	force measured by the load cell in i^{th} direction, $i = x, y, z$
Fr_{xyz}	resultant force
k	reduced frequency, $\bar{c}f\pi/\bar{U}_t$
L	lift force (relative to the wing flight path)
R	wing length, from axis of rotation of the wing to wing tip
Re	Reynolds number
S	total wing surface
T_i	torque measured by the load cell in i^{th} direction, $i = x, y, z$
U_t	wing tip velocity
$\bar{U}_t$	mean wing tip velocity
α	angle-of-attack
$\hat{\omega}$	non-dimensional wing rotation rate, $\bar{c}\,\dot{\alpha}/U_t$
θ_g	gearbox rotation angular displacement or wing cycle angle
θ_w	wing rotation angular displacement
Φ	wing-beat amplitude or stroke angle

1.0 INTRODUCTION

1.1 Project background

The original impetus of this study is rooted in a general effort of the Canadian Space Agency to investigate means for Mars exploration. Rovers are expensive and explore a rather limited area for a given amount of time. Other means of transportation might provide the ability to explore larger areas during the same amount of time at a lower cost. With this in mind, the idea of a number of small flying devices working simultaneously was put forward. The atmospheric density on Mars is about 1% of Earth's density near the surface. This is equivalent to an atmospheric density at an Earth altitude of just over 31km. The use of any fixed-wing aircraft starting from the ground is significantly restricted, as they could not reach the critical speed to create lift at such a low atmospheric density. Fixed-wing aircraft launched from the high atmosphere could fly, since they would be released at high speeds, but very large wings would be required. Insects, on the other hand, set the air in motion around their wings by flapping those wings, therefore allowing flight at much lower Reynolds numbers. As opposed to fixed wing flight starting from the ground, flapping wing flight seems to have better potential for Mars exploration and permit several take-offs and landings to explore a larger area than with a wheeled rover.

While the concept of flapping wings is appealing from an operational point of view, several mechanical challenges were obvious right from the start. Wings flapping up and down are very demanding on the joint section. The reversal motion also induces large strains in the materials of the wings. The Mars atmosphere is so tenuous that even by taking advantage of the flapping motion, large and light weight wings are still required to provide flight. What is explored in this paper is a concept of flapping wings, but the flapping motion is created in one continuous motion, simplifying the demands on the stress levels for both the joints and the wing material. While the concept is very appealing, the effective lift it could deliver had never been explored, as well as the mechanical intricacies required to make the concept functional. A prototype was built and tested in an oil tank. It allowed the examination of the lift mechanisms of this concept, while enabling some improvements to simplify the integration of the parts and detecting difficulties inherent to the concept to reach a fully functional prototype.

This prototype is a unique design, which simplifies the usual 'back and forth' wing motion traditionally needed in order to flap a wing. The mechanism, as well as several adaptations, was invented by Canadian Clément Therriault and has multiple patents[1]. The ingenious design combines two rotational motions that together simulate a flapping-like behaviour; hence the name used here, RotaFlap[2].

The original patent drawings are shown in Fig. 1. The main housing, otherwise described as the rectangular gearbox 32 contains a miter (bevel) gear arrangement, which is shown in detail in the right part of the figure. The housing box rotates in the direction of the motor shaft. The two wings (46 and 48) attached to the gearbox also rotate with respect to the gearbox and in opposite direction relative to each other. The result of the two rotational motions (gearbox and wings), cause the wing tips to trace out a figure-eight like pattern.

There have been three RotaFlap prototype versions (versions, 1.x, 2.0, and 3.0), which have all been derived from the original patent. Some details of these earlier prototypes are given in Refs 2 and 3. In this paper only version 3.0 of the prototype will be discussed. First, the main design features will be introduced. Then, its kinematics will be explored for different sets of parameter. Finally, the experimental set-up will be presented leading to the presentation and discussion of force measurement results.

1.2 Flight modes

Lifting flight modes can be decomposed into three basic categories: fixed-wing, rotary wing and flapping wing; as opposed to other flight sustaining mechanisms such as lighter-than-air or jet-thrust vectoring. Fixed-wing flight distinguishes itself from its two other counterparts by at least two elements. As the name says, the wings are fixed, hence, they do not move relative to the flying vehicle. As a consequence the functions of lift and (forward) thrust are decoupled. Rotary and flapping wings enable an integrated design since these two functions can be accomplished by the same organ. It could be envisaged that, in principle, this merging of the function enabling organs into one may permit some weight saving and increase the vehicle performance. In practice, however, it is not so simple due to the increased complexity of the mechanical system, for one.

Aerodynamic mechanisms, wing motion and wing geometry/number are obviously interdependent. In general, any specific combination of these three elements depends on the mission requirement in the broad sense and on design limitations and constraints. This is true for both man-made vehicles and natural flyers. For instance Woods *et al*[4] analysed power requirements for MAV, i.e. Re ~ 10^5, and concluded that fixed-wing flight is preferable when there is no hover requirement (this conclusion would only be applicable to man-made vehicle since it implies a second organ for propulsion). When there is a hover requirement, their conclusion is that the better choice between flapping or rotary wing depends on mission profile, such as loiter or cruise, and on ambient wind speed.

The primary function of flapping is propulsion or thrust generation. For instance a bird will start to flap its wings when it needs to advance. Otherwise it will stay aloft while soaring using essentially a fixed-wing mode. On the other hand the main function of rotary wings is lift production while hovering. Like helicopters, birds and insects can hover. In doing so, however, the natural flyers must overcome fundamental anatomical and biomechanical limitations since pure continuous rotation is not possible (although not a flyer, the flagellated bacteria can be considered as a notable exception as it uses rotating helical filaments to swim[5]).

Observations of animal hovering have revealed that it can be done in two distinct ways[6,7]. Simplified kinematics are illustrated in Fig. 2. Most insects move their wings on the horizontal plane as shown on the left hand plot of the figure, where the downstroke and upstroke are symmetrical images of each other. The translation phase of each stroke begins and ends with a rapid rotation, known as supination and pronation, around the wing's spanwise axis. The sequence is: downstroke-supination-upstroke-pronation. Seemingly this reciprocating, back-and-forth, symmetrical motion is somehow emulating continuous rotation. Note that the tip of the wings follows a figure-eight like trajectory. This hovering technique is also used by the humming bird, probably simply because its biomechanics permit this motion. For other natural flyers, which are more restricted in their kinematics, the wings are moved up-and-down along an inclined plane in a flapping-like but asymmetrical manner. See the right hand plot in Fig. 2. During the downstroke, a combination of a large amount of drag and some lift is used to generate the required vertical force to balance gravity. During the upstroke, the wings are generally flexed-in in order to minimise energy losses since they serve no significant useful purpose in this part of the cycle, except perhaps to keep its horizontal position.

The specific aerodynamic mechanisms involved in the flapping process are various and complex. The generation of the required vertical force to sustain flapping flight cannot solely be explained by classical lift mechanisms exploited on conventional aircraft. The necessity for lift-enhancing mechanisms is even greater when considering hovering flight, which relies strongly on unsteady aerodynamics[8]. Even though no consensus exists into the exact
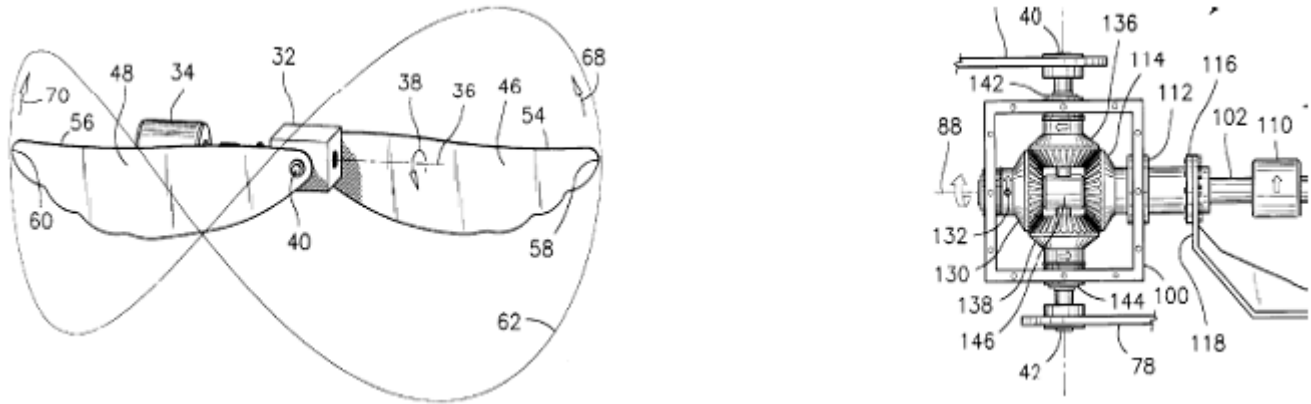
Figure 1. Drawings from original patent: Wing movement for ornithopters and apparatus of the like. Images are from patent document[1].

nature and relative contributions of these aerodynamic effects for flapping flight, a number of phenomena have been identified and studied extensively. For instance, it emerges that the creation of a leading edge vortex (LEV) plays a significant role as a lift-enhancing mechanism. This LEV has often been related to the phenomenon of dynamic stall, first described by Kramer (see Fung[9]) and then studied extensively by McCroskey[10] from the perspective of an airfoil oscillating in pitch in and out of stall. Recently, Wilkins[11] argued that associating the LEV observed in flapping flight with dynamic stall was misleading, pointing out that the dynamic-stall vortex is formed as a translating wing is pitched up, which is not necessarily the case in flapping since the wing usually pitches down at the beginning of each stroke. Exhaustive accounts on the current knowledge of the different aerodynamic mechanisms involved in insect flight can be found in Refs (8, 11 and 12).

A type of motion for which man-made design has had the advantage is pure rotation. As Shyy *et al*[6] put it, continuous circular motion, such as a propeller is rarely found in nature. As mentioned earlier, the flagellated bacteria is one such rare case. In fact the single example that comes to mind of a natural flying vehicle using this motion is the rotary seed[4,13]. Continuous circular motion is perhaps where the RotaFlap design is the most beneficial. It can produce figure-eight like flapping motion kinematics, similar to humming birds, but from pure rotation.

2.0 DESIGN FEATURES

2.1 Gear mechanism

A number of design iterations and modifications were performed before coming up with the final prototype, labeled as RotaFlap version 3.0. The first version was essentially based on the original patent. In conjunction with its integration within the experimental setup, it presented excessive vibrations which ultimately led to version 3.0. It achieves essentially the same wing kinematics as the previous versions but with a different gear arrangement. Figure 3 shows the CAD drawing of RotaFlap v3.0.

At the right side of the figure is the gearbox, which contains a bevel gear arrangement in order to transfer the rotation from the motor to the wings. The wings are not shown here. Only the wing arms pointing up and down from the gearbox are shown. The motor (not shown) is located near the top of the vertical input shaft; only a small portion of the vertical input shaft and beam are seen in the figure. The complete experimental setup is described in Section 4.1. The rotation of the motor is transferred via the 0·25" vertical shaft which transfers the rotation 90° to the hollow steel shaft via a gear arrangement (1:1). The hollow steel shaft directly rotates the gearbox. The steel shaft and rectangular gearbox are rigidly connected. The hollow steel shaft rotates within two through-holes in the *U* bracket where two needle bearings are used.
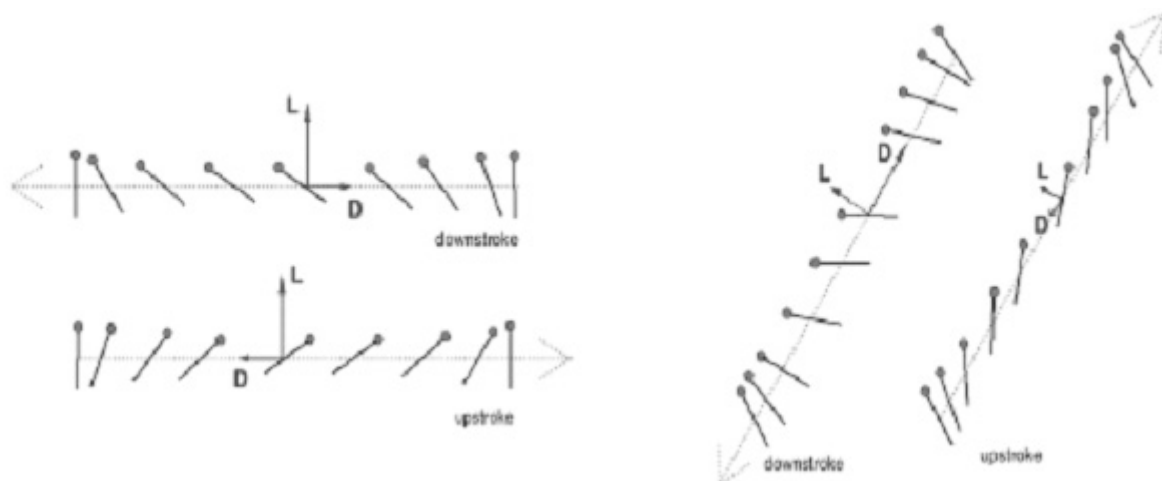

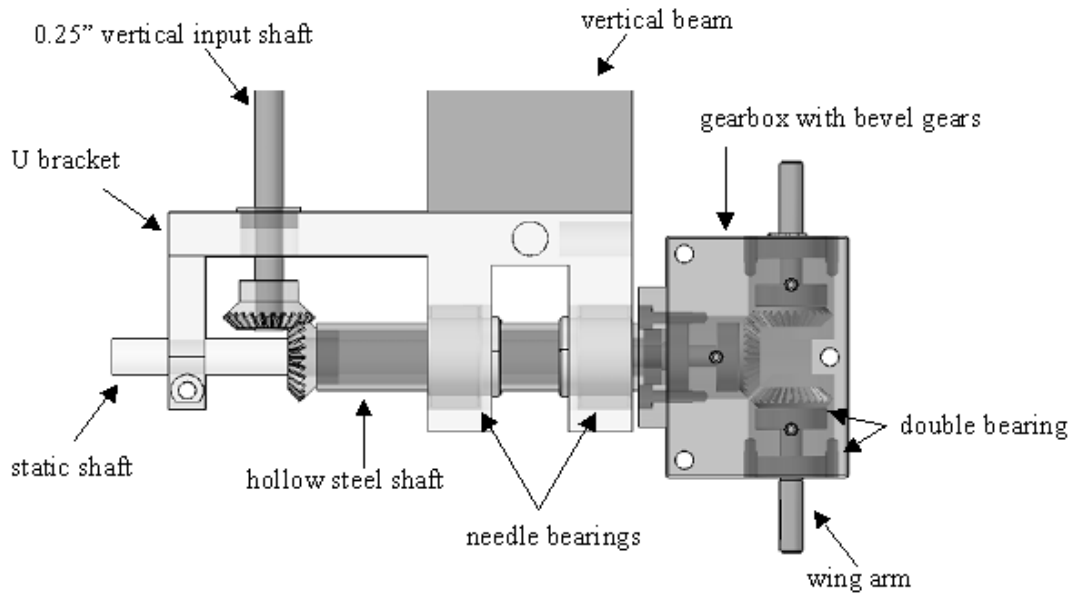Figure 2. Hovering types – (a) normal or symmetrical hovering, (b) asymmetrical hovering.

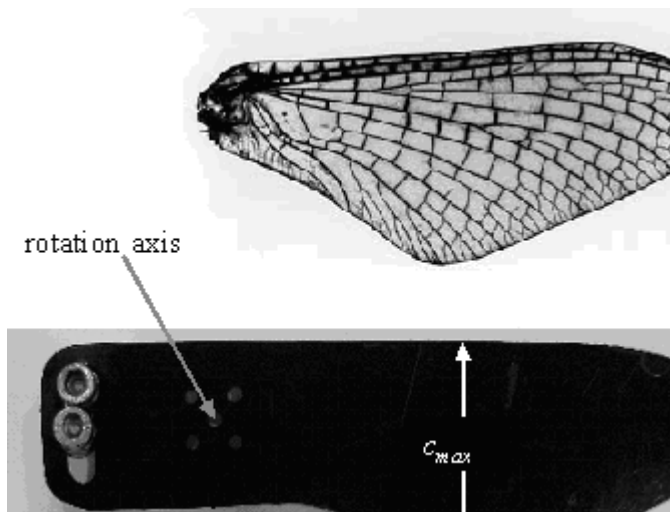Figure 3. Side view (*x-y*) of CAD drawing of RotaFlap v3.0.

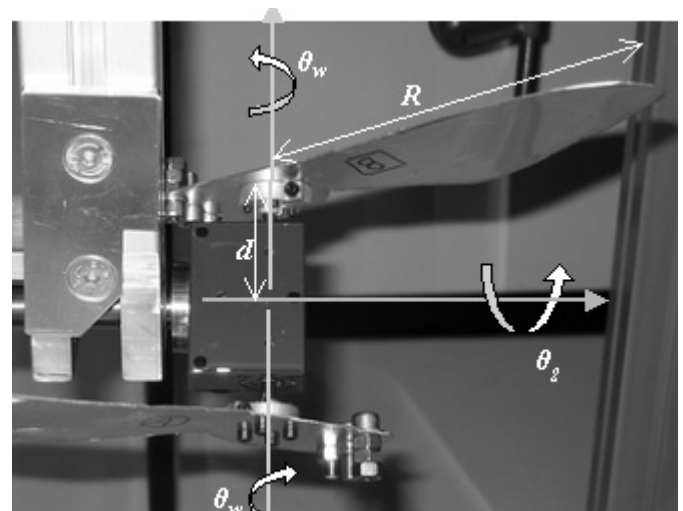Figure 4. RotaFlap wing shape.

Figure 5. RotaFlap kinematic parameters (shown with *R*13 wings).

A much needed modification recommendation from the v1.x prototype was to have multiple bearing supports for the wing arms. Normally this 'Bevel Tee Gearbox' remains stationary as an input shaft transmits rotations (1:1 ratio) to the two output shafts (or wing arms) pointing up and down in the figure. However, by keeping the input shaft stationary and rotating the gearbox instead, the output shafts also rotate. This is exactly what has been done here. The gearbox is rotated by the hollow main steel shaft and the input shaft (defined as static shaft in Fig. 3) is kept static and clamped at the left end onto the *U* bracket, also statically fixed. Thus, the hollow main steel shaft rotates freely about the static shaft that passes within it.

The fact that the gearbox is rotated directly by the hollow steel shaft means that for every one rotation of the hollow steel shaft (one rotation of the motor) there is one rotation of the gearbox. This is not true for v1.x and the original patent. In the original patent the gearbox is rotated indirectly by the main shaft that comes from the motor (equivalent to the hollow steel shaft here). The difference is that in the original patent (v1.x), there are four

gears in the gearbox as shown in Fig. 1 which identifies the gears that are turning with an arrow (#130, #136, #138); the right most gear is static (#114). The main shaft (#102) directly rotates gear #130, which causes gears #136 and #138 to rotate which move about the static gear #114, thus resulting in the gearbox rotating. Essentially the gearbox is indirectly rotated by the motor shaft and resulted in rotational ratio of 2:1. Two complete rotations of the main shaft (or motor) results in one rotation of the gearbox.

In the current v3.0, when the motor rotates one full cycle, the gearbox rotates one full cycle and each of the wings also complete on full cycle of their kinematic wing tip pattern. Since one full cycle of the wing results in two downstrokes and since there are nominally two wings on the prototype, then in one full rotation of the gearbox there are four downstrokes. This constitutes one complete 'flap' cycle in this study; each wing goes through one complete cycle during each rotation of the gearbox. The 'flapping' frequency (*f*) of the RotaFlap is conventionally defined with respect to the rotation of the gearbox. The wing kinematics will be presented in more detail in the next section.

2.2 Wing design

There is an incredible variety of wing shapes in nature, even when examining a particular Re regime. The scope of this study did not include studying different wing types with the RotaFlap wing kinematics. A simple representative insect wing shape was used as shown in the top picture of Fig. 4. This shape is very similar to that of the honeybee wing (*apis mellifera*), which has a very similar chord distribution with respect to the wing length distance[14]. In comparison, a hummingbird wing has its maximum chord at the base of the wing, and the chord decreases fairly linearly towards the wing tip which has a triangular like shape.

This shape was scaled to the appropriate length and was used to cut out a flat-plate wing from a sheet of black Delrin material, as shown in the bottom of the figure. The wing shape with the maximum chord (c_{max}) approximately at half of the wing length location is fairly common in insects. The four holes, in a square formation at $R = 0$, are for the mounting screws onto the wing arm base. The centre hole marks the axis of rotation of the wing with respect to the gearbox. In order to avoid rotational unbalances the wing must be balanced about its axis of rotation. Accordingly, the extra end of the wing contains a slot where nuts and bolts were appropriately positioned to balance the wing about the centre hole. In this study, two main wing lengths (R) were used: 15cm and 17cm. They will be specified by the following short form convention, $R15$ and $R17$, respectively. The two wings with different lengths have identical shapes. For a thickness of 0·23cm and with cmax = 6·8cm, the $R17$ wing has a thickness-to-chord ratio equal to 3%; The R15 wing thickness-to-chord ratio is about 4%.

3.0 KINEMATIC ANALYSIS

3.1 Baseline kinematics

A summary of the parameters that affect the wing kinematics is shown in Fig. 5. The important distances are the wing length (R) and the wing arm distance (d). The wing arm distance is the distance from the axis of rotation of the rectangular gearbox to the wing base. The important angular displacements are the rotation of the gearbox (θ_g) and the rotation of the two wings (θ_w) which rotate relative to the gearbox and opposite to each other. This rotational relationship is due to the internal bevel gear arrangement inside the gearbox presented earlier in Fig. 3. Note that looking down each respective axis, the gearbox angular displacement is positive counterclockwise whereas the wing rotation angle is positive clockwise. The *x-y-z* right-hand coordinate system is fixed with the *x*-axis aligned with the gearbox rotation axis.
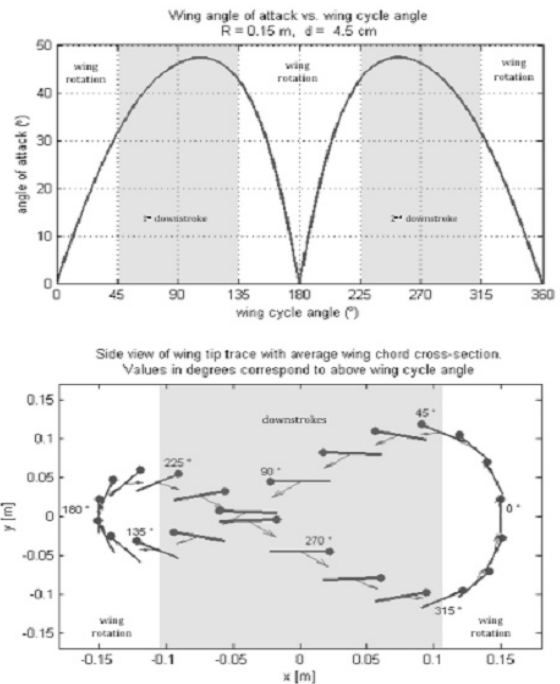

Figure 6. Typical RotaFlap wing kinematics.

The orientation of the coordinate system, with the *y*-axis in the vertical direction, is somewhat arbitrary since the RotaFlap prototype is simply a mechanism by which wings can be moved through space. The optimum orientation of the wing kinematics is not fixed and may not be in the direction presented in this prototype. For instance, should lift production be the main goal, the RotaFlap would have to be oriented in such a way that the dominant forces effectively point in the vertical direction.

The baseline configuration with d = 0·045m and $R15$ wing length results in the figure-eight like wing tip pattern shown in bottom plot of Fig. 6. The plot shows the side view of the wing tip trace, using an average chord cross-section with the circle at the end of the chord line representing the leading edge. The arrows directed from the mid-chord represent the direction the wing is traveling in. The values in degrees correspond to the rotational displacement of the gearbox where one full rotation equals 360°. One full wing cycle corresponds to a 360° rotation of both the wing and the gearbox. The term 'wing cycle angle' will be used in this study to specifically state the rotational position of the gearbox since at each unique rotational position of the gearbox the w ings are also in a unique position within their cycle. Figure 7
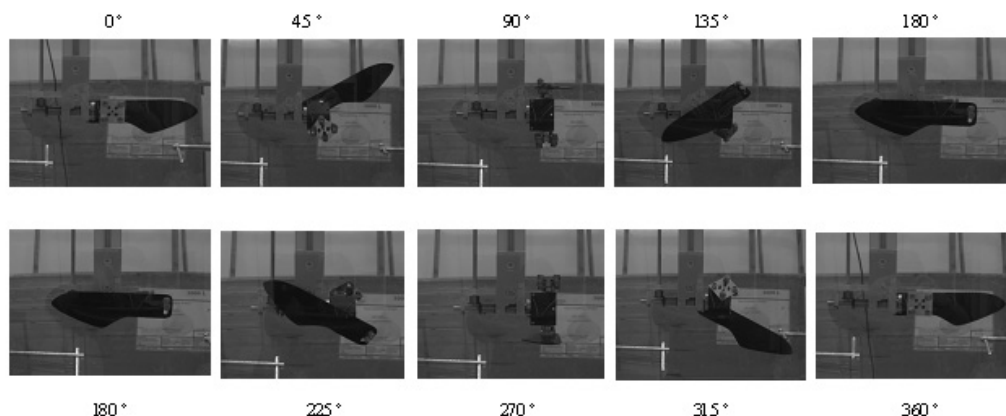

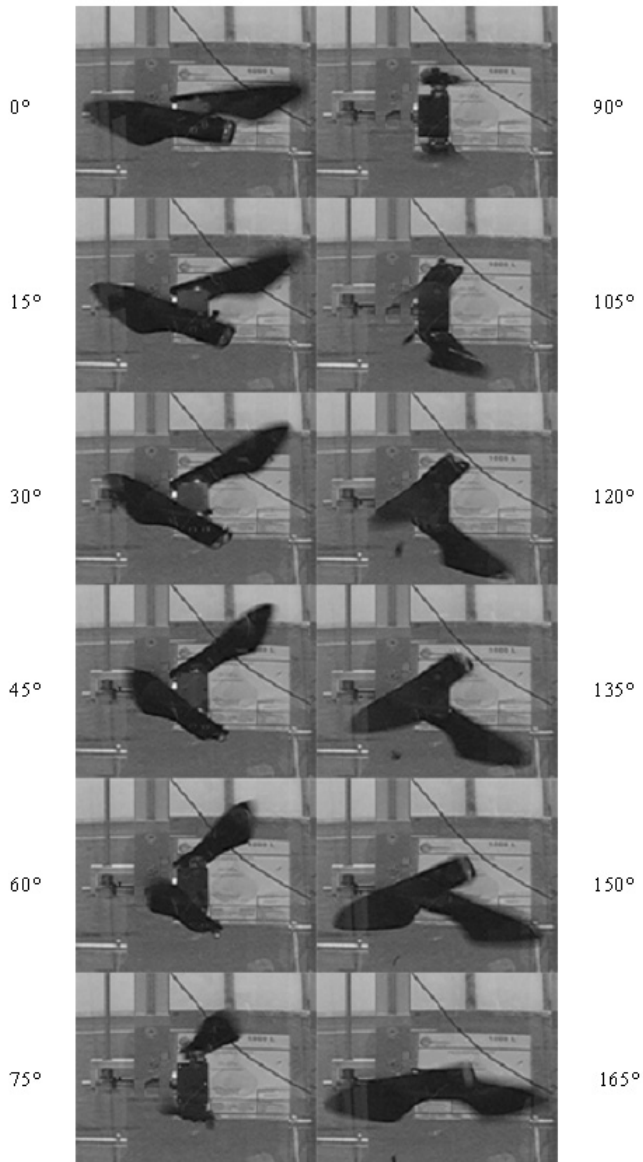Figure 7. Still images (*x-y* view) of one full wing cycle with one wing.

Figure 8. Still images (*x-y* view) of a half-cycle with two wings.

shows different values of gearbox rotation (or wing cycle angle), with one wing attached for a full wing cycle. The second wing, symmetrically mounted as shown in the baseline configuration in Fig. 5, follows the same path with a 180° phase difference. This is shown in Fig. 8 for a half-cycle.

In one full wing cycle, or flapping cycle, each wing has two downstrokes: 1st downstroke is from 45° to 135° and the 2nd downstroke is from 225° to 315°. The geometric angle-of-attack of the wing with respect to the wing direction is plotted *versus* the wing cycle angle in Fig. 6. The maximum geometric angle-of-attack of the wing tip position is a maximum during each respective downstroke. The change in geometric angle-of-attack during one complete wing cycle is mirrored about the 180°degree wing cycle angle, as shown by the plot symmetry in the top plot of Fig. 6.

Normal convention in flapping wing studies is that one wing cycle constitutes a 'back and forth' motion and is comprised of a downstroke and an upstroke. The use of the words 'down' and 'up' is clear for forward flight for birds and insects but not as clear for hovering. The 'downstroke' is conventionally defined as the dorsal to ventral motion of the wing and the 'upstroke' is the ventral to dorsal wing motion. For the RotaFlap wing kinematics presented

here, the convention is that one wing cycle is composed of two similar downstrokes. The RotaFlap is simply a mechanism by which to move wings and hence has no formally defined body and therefore the terms dorsal and ventral have no meaning here.

The wing rotation phase (phase between wing strokes) allows for the wing to move in opposite directions and hence utilises both sides of the wing to be the side that faces down and sees the oncoming airflow. For insects and hummingbirds this phase consists of mainly rotation of the wing, as opposed to both rotation and significant translation (in *y*) as seen in Fig. 6. For instance, during the 2nd rotation phase (from 315° to 45°) the wing translates approximately 1·2 wing lengths in the vertical direction, which is significant compared with hovering insects and hummingbirds.

The non-dimensional wing rotation rate, $\hat{\omega}$, over one full wing cycle for R17 wings at two different wing arm distances ($d = 0·045$ and $0·076$m) is shown in Fig. 9. Note that the wing rotation rate is not to be confused with the flapping frequency, *f*, introduced in Section 2.1. The former is changing with wing cycle angle during one complete cycle, whereas the latter remains constant. For the cases shown in Fig. 9 its maximum value is $\hat{\omega} = 0·56$ for $d = 0·045$, and $\hat{\omega} = 1·05$ for $d = 0·076$. These values are similar to those encountered in fruit-flies, which range from 0 to 0·6[14]. It is believed that values in other insects are larger. A positive $\hat{\omega}$ value represents an increasing angle-of-attack and a negative $\hat{\omega}$ represents a decreasing angle-of-attack. The discontinuities in the plot at 0/360° and 180° are simply a result of the wing changing the side with which it makes the angle-of-attack with its oncoming airflow vector.

The figure-eight wing pattern displayed in Fig. 6, and similarly in Fig. 10, has been noted in insect and hummingbird flight[6,16]. However, as opposed to the RotaFlap pattern which shows significant off-plane displacement (*z* direction Fig. 10) as well as in the *y* direction, natural flyers' figure-eights are usually flatter and thin. Nevertheless, it is not clear how prevalent this pattern is. This has caused much debate since many observations of wing tip kinematics described flat elliptical or parabolic-like non-crossing patterns[17]. The patterns seen in the literature are thought to be dependent on the experimental set up: free flying *vs* tethered insect, abdominal vs. thoracic tether as well as moving air *vs* still air[18].

The wing kinematics in Fig. 10, as well as the following figures, were plotted with the set of equations below which represent the positions of the leading edge ($P_{\mathrm{L.E.}}$), the mid chord ($P_{\mathrm{M.C.}}$) and the trailing edge ($P_{\mathrm{T.E.}}$) of the wing tip (assuming, for visualisation purposes, that it has a finite length equal to the average wing chord) in the *x*, *y* and *z* axes (*i, j, k,* respectively). Hence, the variable, *c*, in Equation (1) is taken as the average wing chord length. The wing angle-of-attack in Fig. 6 was obtained by taking the dot product of the 'chord vector' with the 'direction of travel vector' (arrow vector in Fig. 6 or Fig. 10). It is important to note that the wing tip kinematics presented here assumes no flexibility in the wings.

$$\begin{bmatrix} \overrightarrow{P_{L.E.}} \\ \overrightarrow{P_{M.C.}} \\ \overrightarrow{P_{T.E.}} \end{bmatrix} = \begin{bmatrix} \left(-R\mathrm{Sin}\theta_w - \frac{c}{2}\mathrm{Cos}\theta_w\right) & \left(d\mathrm{Cos}\theta_g - R\mathrm{Cos}\theta_w\mathrm{Sin}\theta_g + \frac{c}{2}\mathrm{Sin}\theta_w\mathrm{Sin}\theta_g\right) & \left(R\mathrm{Cos}\theta_w\mathrm{Cos}\theta_g + d\mathrm{Sin}\theta_g - \frac{c}{2}\mathrm{Sin}\theta_w\mathrm{Sin}\theta_g\right) \\ (-R\mathrm{Sin}\theta_w) & (d\mathrm{Cos}\theta_g - R\mathrm{Cos}\theta_w\mathrm{Sin}\theta_g) & (R\mathrm{Cos}\theta_w\mathrm{Cos}\theta_g + d\mathrm{Sin}\theta_g) \\ \left(-R\mathrm{Sin}\theta_w + \frac{c}{2}\mathrm{Cos}\theta_w\right) & \left(d\mathrm{Cos}\theta_g - R\mathrm{Cos}\theta_w\mathrm{Sin}\theta_g - \frac{c}{2}\mathrm{Sin}\theta_w\mathrm{Sin}\theta_g\right) & \left(R\mathrm{Cos}\theta_w\mathrm{Cos}\theta_g + d\mathrm{Sin}\theta_g + \frac{c}{2}\mathrm{Sin}\theta_w\mathrm{Sin}\theta_g\right) \end{bmatrix} \cdot \begin{bmatrix} \overrightarrow{i} \\ \overrightarrow{j} \\ \overrightarrow{k} \end{bmatrix}$$

. . . (1)

3.2 Parametric study

The wing kinematics presented in the previous figures principally show one particular configuration of the RotaFlap prototype: $R = 0·15$m (R15) and $d = 0·045$m. Altering the wing (*R*) and wing arm (*d*) lengths can produce varying wing tip kinematic patterns. Fig. 11 shows varying views of the mid chord trace pattern at various wing length values with a constant $d = 0·045$m. Figure 12 shows a similar set of plots but with varying d values and a constant $R = 0·15$m. Figure 13, with a similar set of plots, shows different patterns for different values of *R* and *d* while keeping *R/d* constant. A constant *R/d* value allows the wing tip trace to have
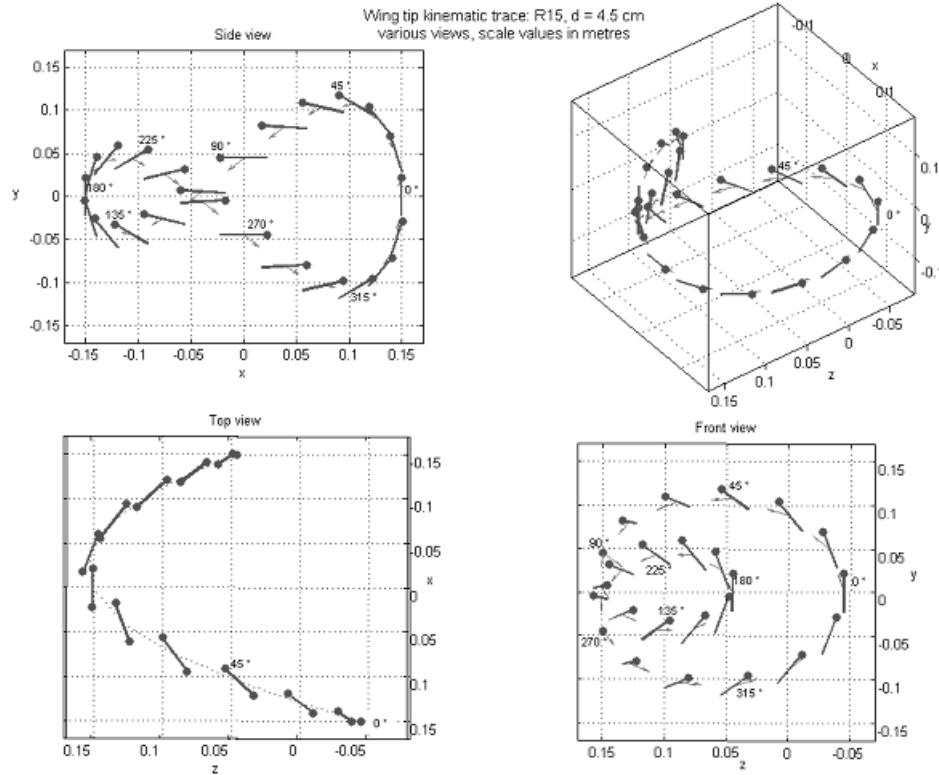
Figure 9. Non-dimensional wing rotation rate during one full wing cycle.
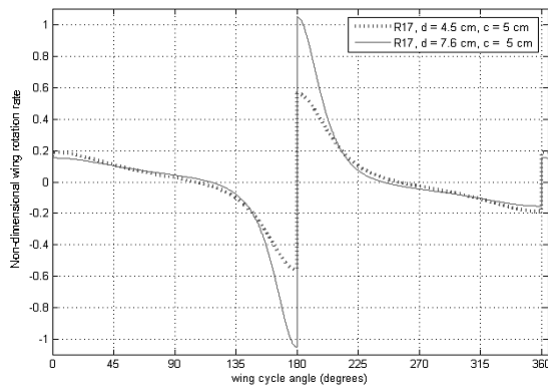

Figure 10. Various views of RotaFlap kinematics.

isometric patterns with varying R and d values.

An interesting observation concerns the case with zero arm length ($d = 0$) shown in Fig. 12. The wing pattern in this particular configuration is nearly identical to the one obtained by Galiński and Żbikowski[19] who used a very intricate double spherical scotch yoke design in order to mimic natural flapping wing flyers, and capable of converting rotary input into reciprocal motion. One of their main design objectives was to obtain a figure-of-eight/banana shape motion on a spherical surface. Very similar kinematics is seemingly obtained by the RotaFlap design but based on a simpler mechanism. The figure-eight motion is observed in the x-y plane and the banana shape in the x-z plane. However, it must be noted by carefully studying Fig. 5 that zero arm length, although possible in theory, is not achievable in practice. Nevertheless, it is conceivable that the arm length, as determined by the gear box size, could be minimised so as to

effectively approach a very similar wing pattern.

The instantaneous angle-of-attack of the wing tip of a $R15$ wing with various wing arm lengths (d) with respect to the wing cycle angle is shown in Fig. 14. The maximum value of the geometric wing tip angle-of-attack is varied from a theoretical $d = 0$m to $d = 0{\cdot}100$m. Increasing the wing arm distance (d) delays the occurrence of the maximum angle-of-attack at a later point in the wing cycle. For instance, for $d = 0{\cdot}100$m the maximum angle-of-attack is reached almost at the very end of the downstroke (wing cycle angle of 135°). Another consequence of increasing d is that the changes in wing angle-of-attack are greater within a smaller wing cycle range, thus resulting in larger non-dimensional wing rotation rates. This characteristic can also be noted from Fig. 9.

Fig. 15 shows the changes of angle-of-attack, at the wing tip, for various wing length values (R). As the wing length is decreased the maximum angle-of-attack increases substantially. For instance for this specific wing arm length ($d = 0{\cdot}045$m), at $R = 0{\cdot}17$m and $R = 0{\cdot}15$m, the maximum angle-of-attack is ∼ 47°, at $R = 0{\cdot}05$ the maximum rises to ∼ 72° and at $R = 0{\cdot}01$ the maximum rises to 180°. This graph can also be interpreted in terms of the local angle-of-attack for a particular wing since the geometric wing angle-of-attack is dependent on the position along the wing. Accordingly, the local geometric angle-of-attack decreases significantly in the spanwise direction.

In summary, the kinematic wing tip patterns, the magnitude of angles of attack, as well as the non-dimensional wing rotation rate for the RotaFlap mechanism share significant similarities with insects and hummingbirds. This would suggest that the RotaFlap's wing motion may produce similar lift coefficients as those found in insects and hummingbirds.
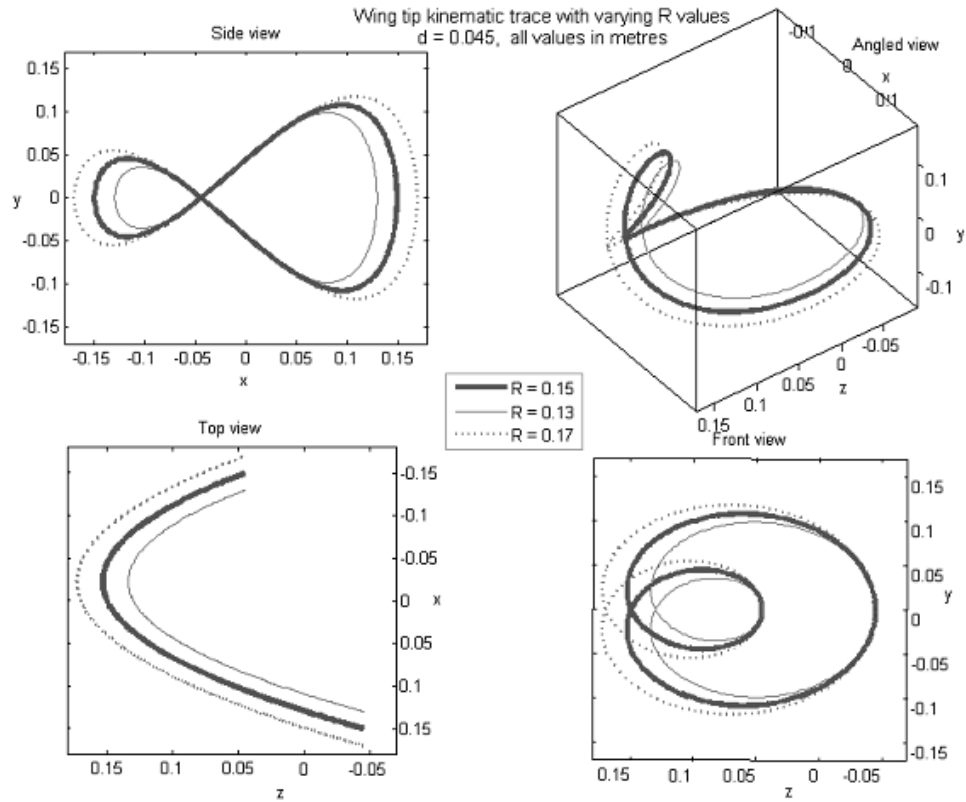
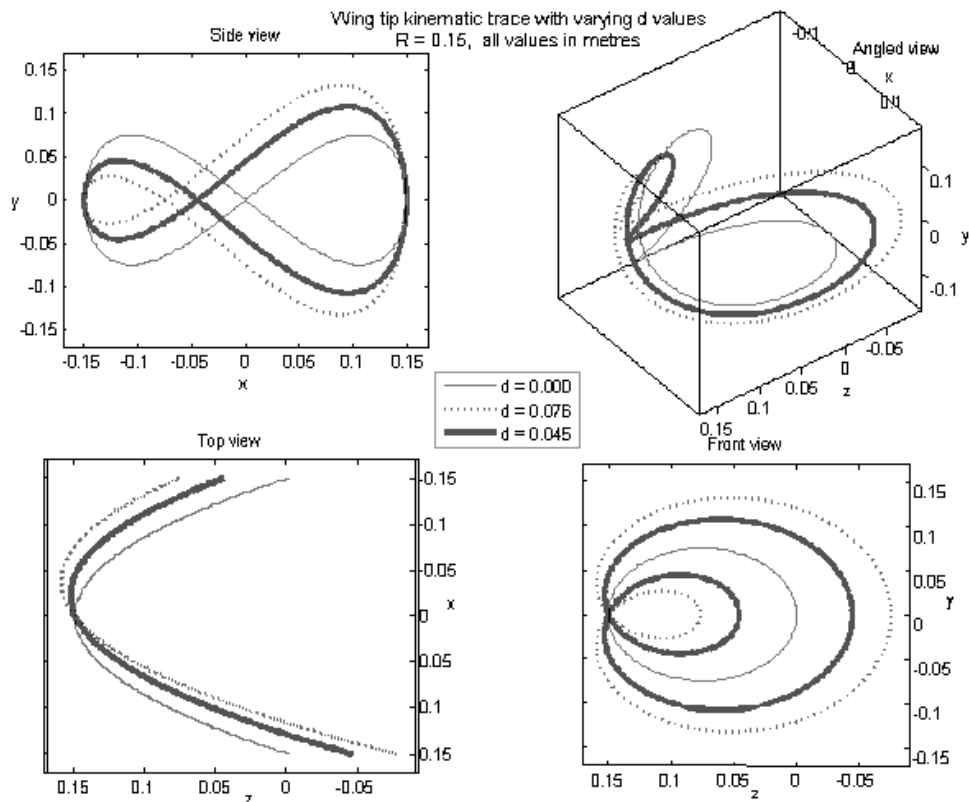Figure 11. Wing tip (mid-chord) pattern for various wing length (*R*) values.

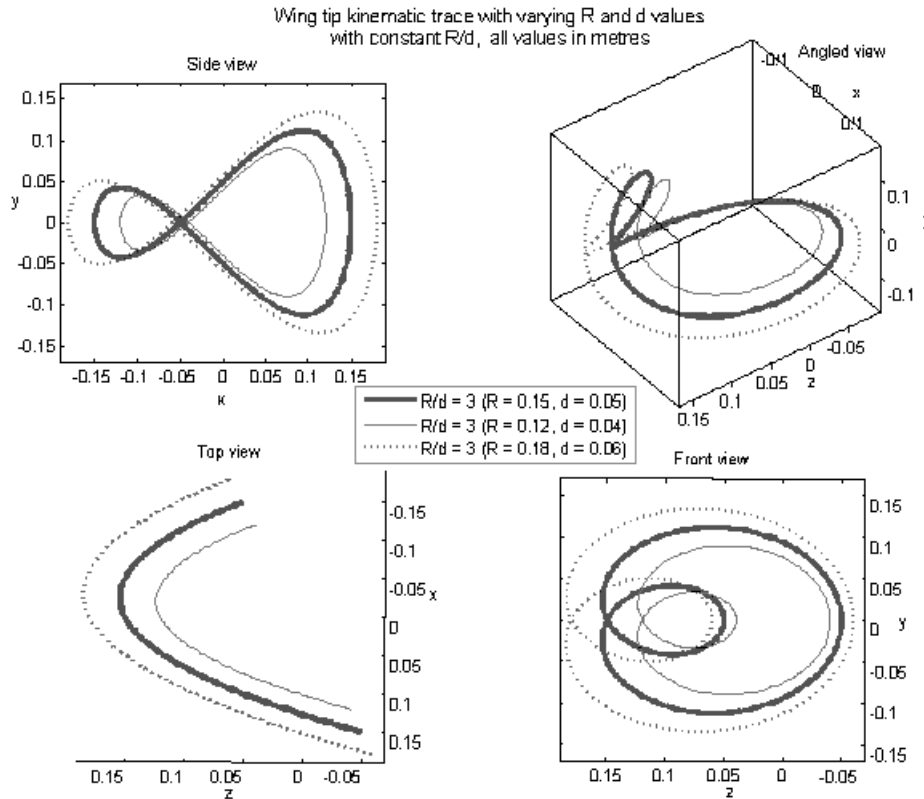Figure 12. Wing tip (mid-chord) pattern for various wing arm (*d*) values.

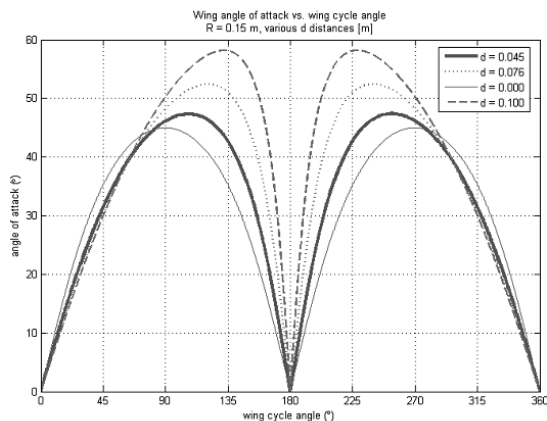Figure 13. Wing tip (mid-chord) pattern for various values of *R/d.*

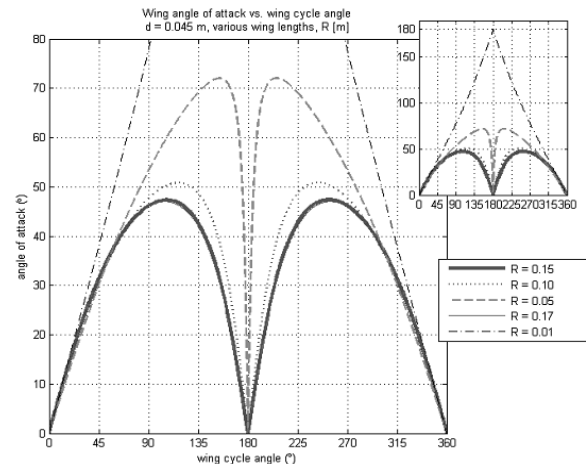Figure 14. Wing angle-of-attack with various *d* values and constant *R* = 0·15m values.

Figure 15. Wing angle-of-attack with various *R* values and constant *d* = 0·045m.

4.0 AERODYNAMIC ANALYSIS

4.1 Experimental set-up

The actual experiment was performed in mineral oil with a kinematic viscosity of v = 20 cSt (or 20×10^{-6} m²/s). It has the same order of magnitude as air. However, its density is 855kg/m³ allowing for much greater aero(fluid)dynamic forces to be measured. This was necessary to increase the signal-to-noise ratio required to use the load cell effectively. The sensing range of the ATI Gamma multi-axis strain gauge based load cell is ±66·7N in force and ± 5·649N·m in torque; its resolution is 55·6mN in F_x and F_y, 111·2mN in F_z and

2·82mN·m in all three torque axes. The overall error, quoted by the company, is 1% full scale value. Using a known mass, static experiments were conducted to test the repeatability and drift errors for this load cell. The resulting errors were not discernable with respect to the load cell resolution values. As well, all load cell errors were found to be lower than the quoted 0·667N maximum overall error from the manufacturer.

The limiting factor for the RotaFlap experimental set-up, which is shown in Fig. 16, is the moments. This is mainly due to the length of the vertical beam required to have the RotaFlap completely submerged and well below the mineral oil surface. Accordingly, the flapping frequency is generally limited to 1·6Hz since above this
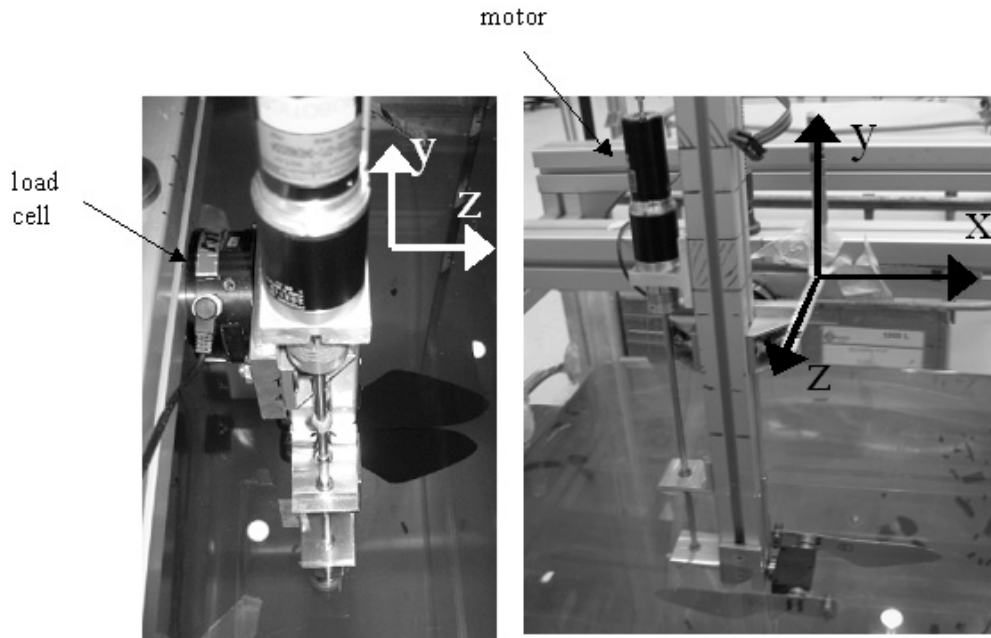
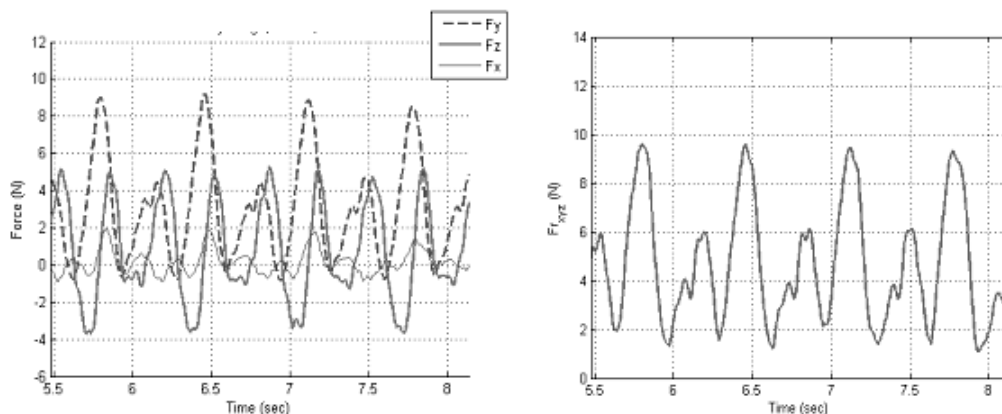Figure 16. Two views of the experimental set-up (different wings are shown in the two views).

Figure 17. Time history of force components (left) and resultant (right); $1R15$, $d = 0.045$m, $f = 1.5$Hz.

value the applied moment exceeds the maximum allowable by the load cell. This value of the maximum flapping frequency also ensures that it is well below the fundamental natural frequency of the beam measured to be 9·1Hz. Assuming a one-degree-of-freedom, second order, system representing the beam, its force transmissibility can be examined. For a measured damping ratio of 0·06, the force magnification factor is 1·032 for an input frequency of 1·6Hz, and the phase shift is 1·3°. These are negligible differences.

The tank size was selected based on the minimum size necessary in order to avoid or limit boundary effects that could alter the aerodynamics, as well as budgetary and resource constraints. Investigation of insect flight studies under similar experimental circumstances aided in the decision making process. Lehmann and Maybury[20] studied the aerodynamics of dragonflies using a scaled robotic model immersed in mineral oil (120 cSt) tank with a cross-section of 0·6 × 0·6m and a height of 1·2m. The wings flapped at 0·533Hz and were 19cm in length. In a similar experiment, Dickinson et al[21] investigated a dynamically scaled model of a fruit fly with a wing length of 25cm and a flapping frequency of 0·145Hz. They used a mineral oil (115 cSt) tank with a conservative size of

1m × 1m × 2m (length × width × height). They also performed boundary effect experiments by incrementally moving the model towards each boundary and recording the measured forces with decreasing distance. These control experiments showed that the sides and surface had minimal influence at distances over 0·5 wing lengths, whereas proximity to the ground was more critical and required a distance of 1·2 wing length to become negligible.

The tank dimensions chosen for this work are 0·6m × 0·6m × 1·2m (length × width × height). Placing the prototype at the centre of the tank results in the following boundary distances (in wing length assuming the nominal $R15$ RotaFlap configuration): Top = 3·22R, Bottom = 3·22R, Sides1 = 0·99R, Sides2 = 1·33R. Notwithstanding the differences between Dickinson et al's experiments and this study, the aforementioned clearances suggest that boundary effects may be negligible. This was confirmed by introducing additional auxiliary walls for each boundary that could be inserted into the tank and systematically repositioned. Based on control experiments with the $R15$ configuration flapping at 1·6Hz, it was concluded that the effect of the side boundaries is negligible above 0·8 wing lengths, the effect of ceiling boundary is negligible above 0·6 wing lengths, and the effect of the ground boundary
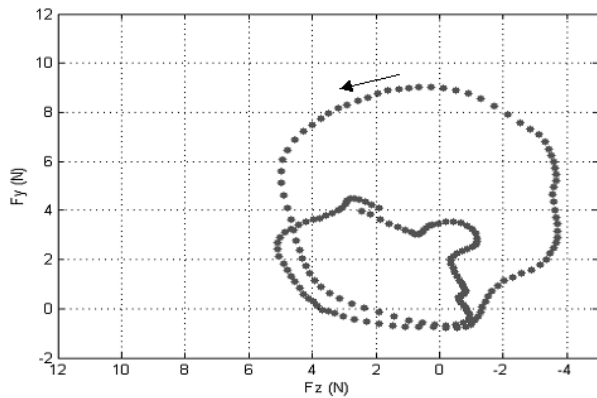
Figure 18. F_y vs F_z magnitude (force vector tip position) for one representative flapping cycle; 1R15, d = 0·045 m, f = 1·5Hz.
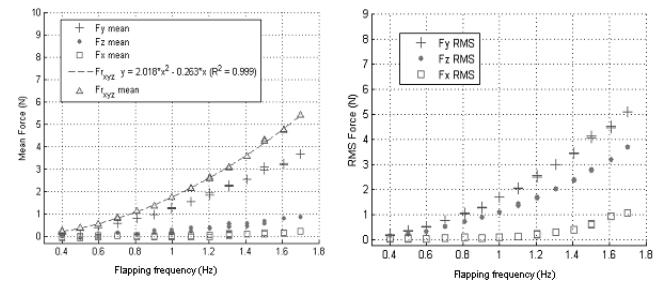

Figure 19. Mean (left) and RMS (right) of force components as a function of flapping frequency; 1R15, d = 0·045m.
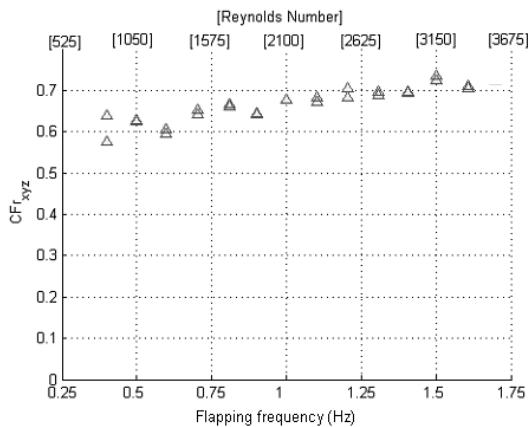

Figure 20. Mean resultant force coefficient as a function of flapping frequency/Reynolds number; 1R15, d = 0·045m.

is negligible above a distance of two wing lengths. Note that these relative clearance distances are larger than the ones used in previous experiments reported in Refs (20 and 21).

Once the motor is turned on, the flow develops very quickly and steady state is obtained after just over one flapping cycle, which corresponds to 2·5 seconds for the smallest frequency tested (0·4Hz). Once steady state is achieved, no appreciable statistical variations in the measured forces are noticed, thus validating the negligible effects of tank confinement and fluid re-circulation. The data used for the analysis was therefore recorded between 5s and 12·5s, hence three cycles of data for f = 0·4Hz and 12 cycles for f = 1·6Hz.

4.2 Force measurements – results and discussion

Before proceedings with the actual experiments, tests were performed with equivalent masses replacing the wings in order to assess the magnitude of the inertial loads. In all cases, the loads measured were of the same order of magnitude as the load cell resolution and well below the load cell error. Accordingly, the inertial loads were deemed not significant and are not considered in the following discussion.

4.2.1 Baseline configuration – 1R15

The first set of results concerns the one R15 wing (1R15) configuration, for which close to four flapping cycles of the three force components are shown on the left plot of Fig. 17, and the resultant

force on the right plot. Note that the force axis scale is different in both. The flapping frequency is 1·5Hz and the data has been filtered using a 2nd order low-pass Butterworth filter with a cut-off frequency of 10Hz. Some peak-to-peak variations are observed but are within the load cell errors discussed earlier.

Each flapping cycle is composed of two peaks since there are two downstrokes per cycle. The difference in magnitude of the two peaks, within one cycle, can be directly related to the asymmetric kinematics ultimately originating from a non-zero value of the wing arm distance, d. See Fig. 12 for which the force time histories of Fig. 17 correspond to the wing kinematics displayed with a thick dark line (d = 0·045), or Fig. 10 which as well illustrates the geometric angle-of-attack. Clearly, the x-component of the force is considerably smaller than the other two. Accordingly, focusing on the two other components the aerodynamic force vector tip position, in the y-z plan, is shown in Fig. 18 for one representative flapping cycle. The arrow shows the direction of time. Note that the max value of the recorded resultant force corresponds to a coefficient of force, CF_r = 0·74.

Statistics of the three force components and their resultant are displayed in Fig. 19 for a range of flapping frequency. Consistent with the time history plot, the x-component is smaller than the other two, most specifically its RMS value. In terms of the mean, the low value of the z-component is to some extent misleading since it has large variations (large RMS) but oscillating about a very small value, as shown in the left plot of Fig. 17.

Focusing on the mean forces, since this is the statistic which has the most direct physical significance for this problem (it is the mean that provides a net vertical force to sustain flight and/or forward force for propulsion), the quadratic behaviour of the mean resultant force suggests that its nondimensional value (force coefficient) is independent of flapping frequency and Reynolds number. This is confirmed by the relatively flat behaviour of the resultant force coefficient shown in Fig. 20, especially for the higher frequencies which tend to level off at CF_r = 0·7 ± 0·02. Note that for flapping frequencies at and below 0·6Hz, Fig. 19 indicates that the mean forces are smaller than the load cell error, hence should be treated with caution.

The Reynolds number is defined in Equation (2), as per Ellington[22]. See also Shyy et al[8] for a more recent, and in some ways more complete, description of the Reynolds number in the context of flapping motion.

$$\mathrm{Re} = \frac{\overline{c}\overline{U}_t}{\nu} \approx \frac{\overline{c}\,2\Phi\,fR}{\nu} \qquad \qquad \ldots (2)$$

$\overline{c}$ is the mean chord and $\overline{U}_t$ is the mean wing tip velocity. The mean wing tip velocity was calculated based on the kinematics equation developed for the RotaFlap, Equation (1). However, a very good
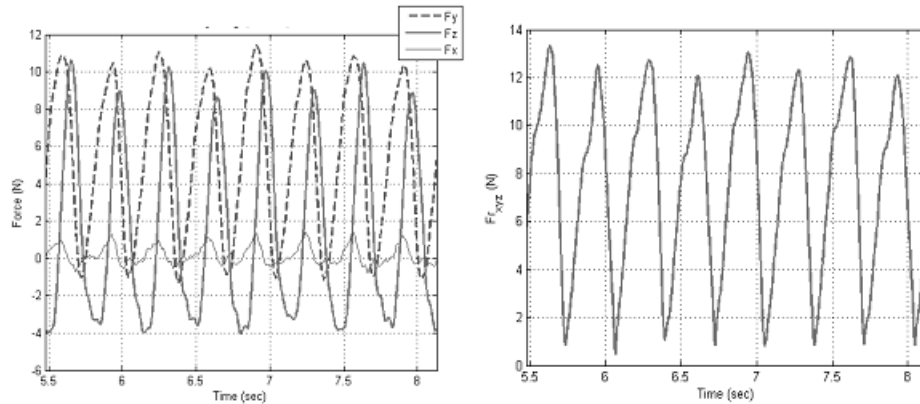
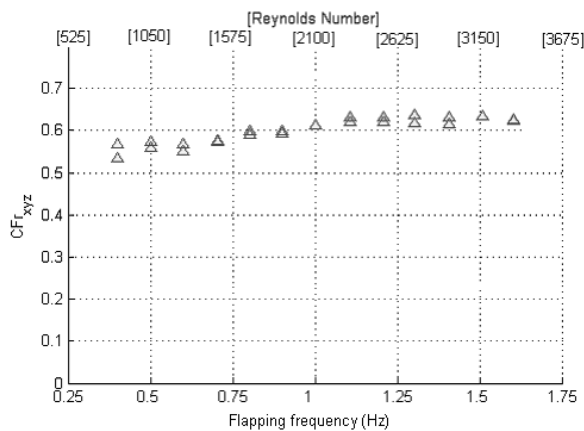Figure 21. Time history of force components (left) and resultant (right); 2R15, d = 0.045 m, f = 1·5Hz.

Figure 22. Mean resultant force coefficient as a function of
flapping frequency/Reynolds number; 2R15, d = 0·045m.

approximation of $\overline{U_t}$ can be obtained with Φ, the wing-beat amplitude or stroke angle in radian, f the flapping frequency in *Hz* and R the wing length as shown in Equation (2) as well. For all cases examined in this work, calculations confirmed the validity of this approximation. The wing-beat angle is the maximum angle that is swept by the wing during one full cycle along its stroke plane. In this case its value is 3·14rads. This is larger but comparable to typical stroke angles found in insects and hummingbirds, which range from 2·0 to 2·6rads[8]. The Reynolds numbers thus obtained for the RotaFlap experiment, as indicated in Fig. 20, are also comparable to those experienced by the bee and the hawkmoth, for instance, but slightly lower than for the hummingbird.

Note that for the hovering case, the reduced frequency given by $k = \overline{c}f\pi/\overline{U_t}$, becomes purely dependant on the wing aspect ratio, $R/\overline{c}$, and is calculated to be 0·167 for the R15 wing. This value of reduced frequency represents an intermediate case between typical hovering large scale helicopter rotation frequencies ($k < 0·1$) and beating wings of hovering insects ($k > 0·2$)[7].

4.2.2 Baseline configuration with two wings – 2R15

Adding the second wing, symmetrically mounted as shown in Fig. 5, results in the following force time history (see Fig. 21). The dominant force components as still F_y and F_z. In theory, the two half-cycle peaks should be the same since both wings follow exactly the same path but one lagging the other by 180°. The slight difference is attributed to a small bending deformation of one wing.

The mean force components and resultant are larger than for the single wing configuration, as expected. However, expressed in nondimensional form as shown in Fig. 22, the mean of the resultant force is slightly lower than for the single wing configuration. It suggests that there exist some negative interference effects between the two wings. The same observation was noted when comparing the larger R17 wing with the 2R17 configuration. In average, the two-wing case displayed a mean resultant force coefficient 10% lower than the single wing. On the other hand, the addition of a wing spacer to increase the wing arm distance from the baseline value, d = 0·045m, to d = 0·076m, hence potentially decreasing wing-to-wing interference effects, did not show any significant impact on the mean resultant force. However, it must be noted that changing the parameter, d, has more than one effect, as discussed in Section 3.2. These different effects could cancel each other out. In this regard, an in-depth aerodynamic analysis would be required in order to better understand the relative contribution of each effect.

The coefficients of force obtained with the RotaFlap in hovering like conditions can be compared with the hummingbirds'. Chai and Millard[23] measured the hovering performance of four different types of hummingbirds. Based on the following approximated expression for the mean wing tip speed, $\overline{U_t} = 2\Phi fR$, and the measurement of the wing-beat amplitude, flapping frequency and wing length, as well as the mean chord and birds' weight, the coefficients of force calculated range from 0·35 to 0·41 in hover. The hummingbirds can generate much larger force coefficients during maneuvering flights. Nevertheless, these values are comparable to the RotaFlap's. The corresponding Reynolds number is approximately 10^4, which is about twice the values of Re tested with the RotaFlap. A similar comparison with hovering insects, based on Weis-Fogh measurements[24], indicates a comparable range of force coefficients, 0·3 ~ 0·7, at the same Reynolds numbers and lower.

5.0 CONCLUSION

The RotaFlap is a relatively simple design, which in many ways, emulates the general figure-eight wing kinematics pattern of insects and hummingbirds. The pseudo-flapping motion is achieved with pure rotation of all the parts involved, hence is likely to have some efficiency benefits compared with other flapping mechanisms. For the configurations and flight conditions studied, this design has demonstrated that it can rival aerodynamically with insects and birds in the same range of Reynolds numbers. Specifically, its kinematic wing tip patterns, magnitude of angles of attack, as well as its non-dimensional wing rotation rates share significant similarities with natural flyers. It is therefore not surprising that the RotaFlap's wing motion produces similar values of lift coefficient to those found in insects and hummingbirds.

ACKNOWLEDGEMENTS

REFERENCES

1. THERRIAULT, C. and THERRIAULT, M. U.S. Patent #6,227,483 B1 8 May 2001; Canadian Patent #2,304,892, 8 November 2004.
2. DESMARAIS, G. Martian flight study: prepared for the Canadian Space Agency, M.S. project, Concordia University, Montreal, Canada, 2003.
3. ANIA, A., POIREL, D., POTVIN, M.J. and MONTMINY, S. Flapping wing devices for mars exploration, *J Engineering Design and Innovation*, 2005, **1P**, pp 1-8.
4. WOODS, M.I., HENDERSON, J.F. and LOCK, G.D. Energy requirements for the flight of micro air vehicles, *Aeronaut J*, 2001, **105**, (1045), pp 135-149.
5. BERG, H. The rotary motor of bacterial flagella, *Annual Review of Biochemistry*, 2003, **72**, pp 19-54.
6. SHYY, W., BERG, M. and LJUNGQVIST, D. Flapping and flexible wings for biological and micro air vehicles, *Progress in Aerospace Sciences*, 1999, **35**, pp 455-505.
7. SANE, S. The aerodynamics of insect flight, *J Experimental Biology*, 2003, pp 4191-4208.
8. SHYY, W., LIAN, Y., TANG, J., VIIERU, D. and LIU, H. *Aerodynamics of Low Reynolds Number-Flyers*, Cambridge University Press, Cambridge, UK, 2008.
9. FUNG, Y.C. *An Introduction to the Theory of Aeroelasticity*, John Wiley & Sons, New York, USA, 1955.
10. MCCROSKEY, W.J. The Phenomenon of Dynamic Stall, NASA TM 81264, 1981.
11. WILKINS, P.C. Some Unsteady Aerodynamics Relevant to Insect-Inspired Flapping-Wing Micro Air Vehicles, PhD thesis, Cranfield University, Shrivenham, UK, 2008.
12. SHYY, W., AONO, H., CHIMAKURTHI, S.K., TRIZILA, P., KANG, C.-K., CESNIK, C.E.S. and LIU, H. Recent Progress in Flapping Wing Aerodynamics and Aeroelasticity, Progress in Aerospace Sciences, 2010, doi:10.1010/j.paerosci.2020.01.001.
13. AZUMA, A., OKAMOTO, M. and YASUDA, K. *Aerodynamic characteristics of wings at low Reynolds number, Fixed and Flapping Wing Aerodynamics for Micro Air Vehicle Applications*, MUELLER, T. (Ed) AIAA, 2001.
14. ALTSHULER, D.L., DICKSON, W.B., VANCE, J.T., ROBERTS, S.P. and DICKINSON, M.H. Short-amplitude high-frequency wing strokes determine the aerodynamics of honeybee flight, PNAS, 2005, **102**, (50), pp 18213-18218.
15. SANE, S.P. and DICKINSON, M.H. The aerodynamic effects of wing rotation and a revised quasi-steady model of flapping flight, *J Experimental Biology*, 2002, **205**, pp 1087-1096.
16. MAXWORTHY, T. The fluid dynamics of insect flight, *Annual Review Fluid Mech*, 1981, **13**, pp 329-350.
17. WANG, Z.J. Dissecting insect flight, *Annual Review Fluid Mech*, 2005, **37**, pp 183-210.
18. SANE, S.P. and DICKINSON, M.H. The control of flight force by a flapping wing: lift and drag production, *J Experimental Biology*, 2001, **204**, pp 2607-2626.
19. GALIŃSKI, C. and ŻBIKOWSKI, R. Insect-like flapping wing mechanism based on a double spherical Scotch yoke, *J R Soc Interface*, 2005, **2**, pp 223-235.
20. LEHMANN, F. and MAYBURY, W.J. The fluid dynamics of flight control by kinematic phase lag variation between two robotic insect wings, *J Experimental Biology*, 2004, **207**, pp 4707-4726.
21. DICKINSON, M.H., LEHMANN, F. and SANE, S.P. Wing rotation and the aerodynamic basis of insect flight, *Science*, 1999, **284**, pp 1954-1960.
22. ELLINGTON, C.P. The aerodynamic of hovering insect flight. VI. Lift and power requirements, *Phil Trans R Soc Lond*, 1984, B **305**, pp 145-181.
23. CHAI, P. and MILLARD, D. Flight and size constraints: Hovering performance of large hummingbirds under maximal loading, *J Experimental Biology*, 1997, **200**, pp 2757-2763.
24. WEIS-FOGH, T. Quick estimates of flight fitness in hovering animals, including novel mechanisms for lift production, *J Experimental Biology*, 1973, **59**, pp 169-230.

www.aerosociety.com
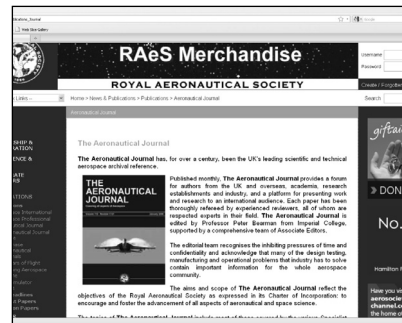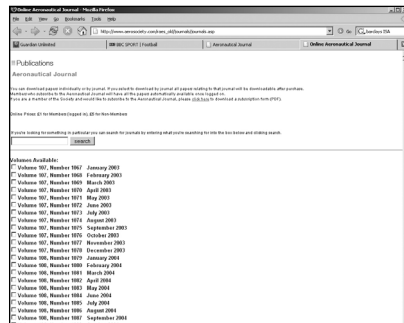
The Aeronautical Journal is now accessible on the RAeS website. All papers published from January 2003 can be viewed and downloaded for free by subscribers and for a small fee by all others.

The latest aerospace news can also be found every day on the RAeS website.

The website has an online news service featuring extended coverage of the latest aerospace, air transport, defence, space and general aviation news.

These news pages are updated each weekday by our editorial news team and include many items which, for reasons of space, do not appear in the magazine. An archive of previous news stories can also be accessed by Society members.

The RAeS website also contains information on all of the Society's activities, including publications, membership, Divisions, Branches, conferences, careers, awards and library services.

Online Prices: Journal Paper £1 for members, £5 for Non-Members

Whole Journal issue £5 for members, £30 for Non-Members

Free to subscribers
Please note that subscribers will be required to submit their computer's IP address(es) in order to gain free access to each monthly edition of *The Aeronautical Journal* and the complete archive of *The Aeronautical Journal* papers at the RAeS website.
Subscribers should send their IP address(es) (with subscription number) to David Thomas at: ras@servicehelpline.co.uk